JGR Atmospheres

RESEARCH ARTICLE
10.1029/2025JD044387

Radar Observations of Inner Rainband Contributions to Eyewall Formation During the Rapid Intensification of Typhoon Cempaka (2021)

Xueqi Fan[1,2], Jie Ming[1,2], Qingqing Li[3], Kun Zhao[1,2], Hao Huang[1,2], Ming Xue[4], Yihong Duan[5], and Dajun Zhao[5]

[1]State Key Laboratory of Severe Weather Meteorological Science and Technology, Nanjing University, Nanjing, China, [2]Key Laboratory of Mesoscale Severe Weather/Ministry of Education, School of Atmospheric Sciences, Nanjing University, Nanjing, China, [3]Key Laboratory of Meteorological Disaster of the Ministry of Education, Nanjing University of Information Science and Technology, Nanjing, China, [4]Center for Analysis and Prediction of Storms, and School of Meteorology, University of Oklahoma, Norman, OK, USA, [5]Chinese Academy of Meteorological Sciences, China Meteorological Administration, Beijing, China

Key Points:

- Radar observations revealed that inner rainbands contributed to the eyewall formation of Cempaka
- Strain-generated and vortex Rossby wave-coupled bands were observed
- Inner rainbands were active inside and outside the radius of maximum winds during different stages

Correspondence to:
J. Ming,
jming@nju.edu.cn

Citation:
Fan, X., Ming, J., Li, Q., Zhao, K., Huang, H., Xue, M., et al. (2025). Radar observations of inner rainband contributions to eyewall formation during the rapid intensification of Typhoon Cempaka (2021). *Journal of Geophysical Research: Atmospheres*, *130*, e2025JD044387. https://doi.org/10.1029/2025JD044387

Received 21 MAY 2025
Accepted 11 NOV 2025

Abstract This study utilizes coastal radar observations to investigate eyewall formation processes during Typhoon Cempaka's (2021) rapid intensification. Two distinct types of inner rainband governed the evolution of eyewall formation: (a) strain-generated bands forming inside the radius of maximum winds (RMW) through cellular convection, and (b) vortex Rossby wave-coupled bands developing outside the RMW via convergence-driven convection. When strain-generated bands dominated near the RMW, a mean tangential wind tendency budget indicates that enhanced convection inside the RMW contributed to net spin-up at lower levels, promoting RMW contraction. Meanwhile, the prevalence of wave-coupled bands beyond the RMW led to significant wind acceleration near and outside the RMW, primarily driven by symmetric contributions. The axisymmetrization of these inner rainbands ultimately resulted in eyewall formation. These radar-based findings underscore the critical role of inner rainbands in eyewall formation, contrasting with previous studies that emphasize outer rainbands.

Plain Language Summary When typhoons and hurricanes grow stronger, their most destructive winds develop in a ring-shaped zone called the "eyewall" around the storm's center. Considerable efforts have been focused on the formation processes and mechanisms of eyewalls. This research analyzed Typhoon Cempaka—a small, slow-moving storm that hit China in 2021—using detailed weather radar observations along the coast. We discovered two different patterns that worked together to build the typhoon's eyewall. The first involved clusters of thunderstorms. The second pattern occurred farther from the storm's core, related to a long-lived, well-organized series of thunderstorms. These observations also reveal how complex interactions between different parts of a storm contribute to its intensification.

1. Introduction

Over the past few decades, while steady though relatively modest progress has been made in understanding and predicting tropical cyclone (TC) intensity changes (Cangialosi et al., 2020; Chen et al., 2023; Gall et al., 2013; Rappaport, 2009), accurate forecasting of significant intensity changes, for example, rapid intensification, remains a substantial challenge (Fischer et al., 2025; Kaplan et al., 2015; Rozoff et al., 2015). Previous studies indicate that varying internal processes related to TC structures are commonly responsible for the TC intensity change (Hendricks et al., 2010; Wu et al., 2016), including the structural change in the eyewall characterized by a closed or partially-closed convective ring near the radius of maximum winds (RMW) from a precipitation perspective. Key processes such as eyewall formation, eye–eyewall mixing (Kossin & Eastin, 2001; Sitkowski et al., 2011), and eyewall replacement cycles (Black & Willoughby, 1992; Cha et al., 2021; Didlake et al., 2017; Kossin & DeMaria, 2016; Sitkowski et al., 2011; Willoughby et al., 1982) have been shown to substantially influence TC intensity changes.

For example, eyewall formation—a convective ring-like structure that gradually develops near the RMW—can likely be attributed to the convective axisymmetrization processes (Chen, 2018; Chen et al., 2018; Miyamoto & Takemi, 2013; Nguyen & Molinari, 2012; Shimada et al., 2017). These axisymmetrization processes are closely

linked to significant TC intensity changes (Chen, 2018; Chen et al., 2018; Miyamoto & Takemi, 2013; Shimada et al., 2017). Within these processes, diabatic heating drives a secondary circulation that transports angular momentum inward, accelerating the primary circulation. The resulting increase in tangential winds enhances inertial stability, improving the conversion efficiency from potential to kinetic energy (Schubert & Hack, 1982; Shapiro & Willoughby, 1982). Both theoretical and observational studies (Nolan et al., 2007; Pendergrass & Willoughby, 2009; Schubert & Hack, 1982; Shapiro & Willoughby, 1982; Vigh & Schubert, 2009) suggest that TC intensification is more efficient when diabatic heating occurs inside the RMW, where inertial stability is higher. As a result, eyewall formation processes have long been one of the key focuses in TC dynamics research.

Observationally, distinct convective features are associated with the process of eyewall formation in TCs. For example, based on satellite-derived brightness temperature data, Chen and Wu (2022) proposed two primary patterns of TC eye (equiv. eyewall) formation: the clearing-type formation and the banding-type formation. In the clearing-type formation scenario, this concept denotes the evaporation and subsequent dissipation of the deep convective activity that is initially concentrated in the vicinity of the center of the central dense overcast. Conversely, the banding-type formation is characterized by the aggregation and subsequent envelopment of the storm center by a curved banding structure. The findings about the two types of eye formation are in consonance with those put forth by Vigh et al. (2012), whose research was founded on aircraft reconnaissance data. A difference in diabatic heating patterns is postulated to exist between these two formation mechanisms. In the context of clearing-type formation, it is hypothesized that a certain degree of diabatic heating is likely to occur within the RMW. By contrast, in the case of banding-type formation, the convectively-induced diabatic heating typically shows an inclination to take place outside the RMW. Furthermore, Chen and Wu (2022) documented that TCs experiencing clearing-type eye formation demonstrate significantly enhanced intensification rates. Their subsequent investigation (Chen & Wu, 2025) revealed the critical role of overshooting convection in driving the accelerated intensification processes, particularly in smaller TCs predominantly characterized by clearing-type eye formation.

Typhoon Cempaka (2021), a compact TC, underwent RI shortly before making landfall in Guangdong Province, China. Cempaka originated in the vicinity of the southeastern coast of China (not shown), and its RI was concurrent with the formation of the eyewall as the storm migrated westward. The Doppler radars installed in the coastal area offer a valuable opportunity to monitor the eyewall formation process during Cempaka's RI. Specifically, the fine-scale convective features associated with the eyewall formation can be precisely delineated. These features are scarcely discernible in infrared satellite data because of the obstruction caused by cirrus anvils in the outflow layer. This study intends to employ ground-based dual-Doppler radars to comprehensively characterize the convective structures of Typhoon Cempaka (2021) during the eyewall formation stage within the RI period.

The remainder of the paper is organized as follows. Section 2 describes the observation instruments, quality control processes for the data, and analysis methodology. The eyewall formation mechanisms of Typhoon Cempaka (2021) are discussed in Section 3. Conclusions with additional discussions are given in Section 4.

2. Data and Methods

Cempaka, the seventh typhoon in the 2021 season and the first to make landfall along the Chinese coast this year, inflicted devastating gales and torrential rainfall upon the coastal region. Originating in the South China Sea on 18 July 2021, the typhoon commenced a gradual northwestward track toward the coast of Guangdong. Subsequently, on July 19, it experienced an RI process, attaining typhoon category. At around 1800 UTC, it reached its peak intensity, characterized by a maximum sustained (2-min average) wind speed of 38 m s^{-1} near the center.

Dual coastal S-band Doppler radars located at Yangjiang (YJ) and Zhuhai (ZH), China, captured the eyewall formation of Typhoon Cempaka (2021) during its pre-landfall phase along the Guangdong coast (Figure 1). The radar network achieved full volumetric coverage of the TC's inner-core region through high-temporal-resolution scanning (6-min intervals), with a maximum effective Doppler velocity detection range of 230 km. The observational framework employed a multi-elevation scanning strategy spanning 0.5°–19.5° across nine discrete elevation angles, enabling three-dimensional kinematic characterization of convective structures within the inner core (within three times the RMW) of the typhoon.

Figure 1a presents two tracks obtained from different methodologies: the best-track and dynamic centers. The Chinese Meteorological Administration pinpointed the best-track centers every 3 hours by integrating data from

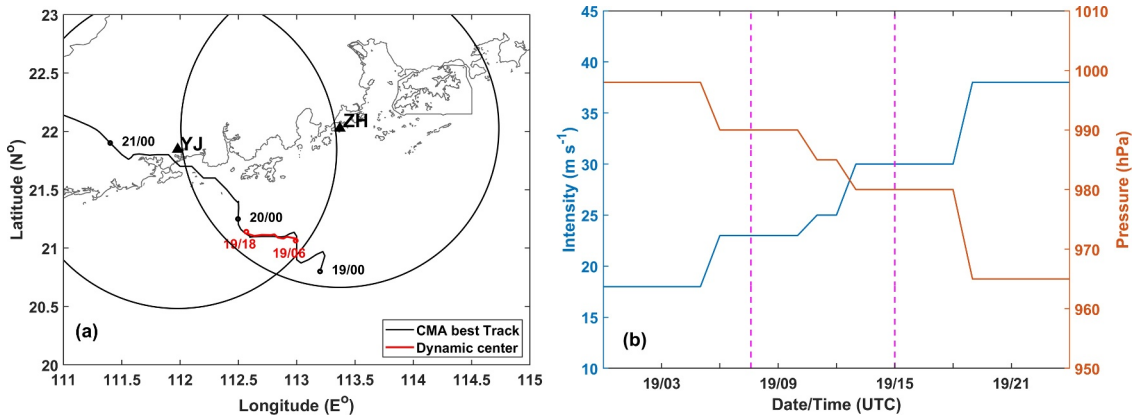

Figure 1. (a) Two tracks of Typhoon Cempaka derived from the Chinese Meteorological Administration best track (black) from 0000 UTC, 19 July to 0000 UTC, 22 July and dynamic centers (red) from 0600 UTC to 1800 UTC on 19 July. (b) Time evolution of maximum surface wind (blue line) and minimum sea level pressure (orange line) of Cempaka. Dashed magenta lines indicate the period of RI of interest.

radar, satellite observations, in situ measurements, and sounding data. In contrast, the dynamic centers were defined as the center of the vortex extracted from the wind circulation at the 2-km constant altitude plane position indicator. This was achieved by utilizing the intersections of bearings normal to the wind directions across the center, following the approach described by Willoughby and Chelmow (1982). A noteworthy parallelism can be discerned between the trends of these two tracks. Figure 1b depicts the intensity evolution based on the Chinese Meteorological Administration best-track data. From 0000 UTC on 19 July to 0000 UTC on 20 July, the minimum sea-level pressure underwent a decline from 998 to 965 hPa. Concurrently, the near-surface 2-min mean maximum wind witnessed an increment of 20 m s^{-1} over a 24-hr span. In line with the conventional definition of RI, where the maximum wind speed escalates by more than 15.4 m s^{-1} within 24 hr (Kaplan & DeMaria, 2003), it is evident that Cempaka experienced RI during this period. It is important to note that the principal analysis timeframe of this study spans from 0730 to 1500 UTC on 19 July 2021 (marked by magenta dashed lines in Figure 1b; hereafter, all times pertain to UTC on 19 July 2021). During this specific time interval, Cempaka was in the nascent stage of this RI event, as illustrated in Figure 1b.

The radar data from the YJ and ZH radars underwent initial objective correction via the region-based dealiasing method accessible within the Python-ARM Radar Toolkit (Helmus & Collis, 2016). Subsequently, non-meteorological echoes were removed through manual processing using the National Center for Atmospheric Research Solo II software (Oye et al., 1995). To obtain a more regular data structure, the Doppler radial velocities were interpolated onto a Cartesian grid with dimensions of 1 km × 1 km × 0.5 km. This interpolation was accomplished by employing the "REORDER" software developed by the National Center for Atmospheric Research (Oye & Case, 1995). Then, three-dimensional wind fields were obtained using the Custom Editing and Display of Reduced Information in Cartesian space (Mohr et al., 1986). The dual-Doppler lobe covered a substantial portion of the inner core of Cempaka. This coverage facilitated an in-depth examination of the fine structures within the inner rainbands. Given that Cempaka was a small-scale typhoon, the environmental wind shear related to it was precisely defined as the vector difference between the wind vectors averaged over a relatively confined region. Specifically, these averages were calculated for the radial distance ranging from 200 to 400 km from the storm center at 200 and 850 hPa. The wind fields used for this calculation were sourced from the fifth-generation European Center for Medium-Range Weather Forecasts reanalysis (ERA5; . The analysis results indicated a southeasterly wind shear with a magnitude of less than 5 m s^{-1} during the period of investigation, as shown in Figures 2a–2c.

3. Results

Figures 2a–2d depict the radar reflectivity at an elevation of 1.5° at 2-hour intervals from 0800 UTC to 1400 UTC. Throughout this time frame, the inner core (Houze, 2010) underwent a remarkable transition from an azimuthally asymmetric configuration to a symmetric one. At 0800 UTC, two distinct banded structures emerged near the storm center. Specifically, one banded structure was located on the northern side, while the other was situated on

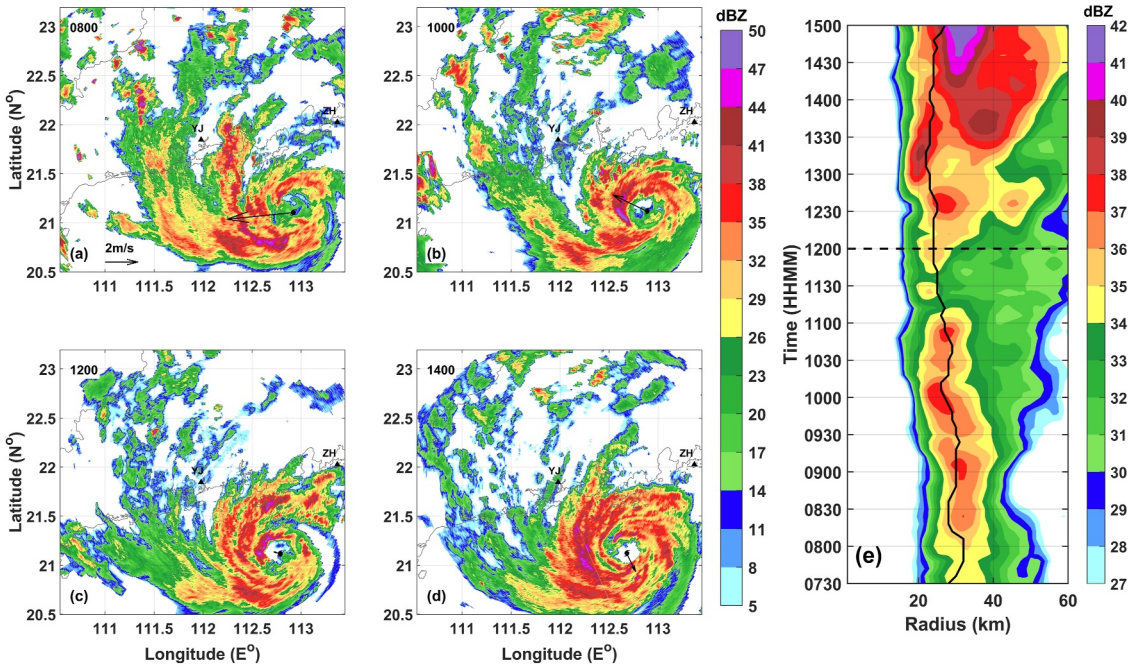

Figure 2. Radar reflectivity (shading; dBZ) of Typhoon Cempaka at 1.5° elevation was observed by YJ radar at (a) 0800, (b) 1000, (c) 1200, and (d) 1400 UTC. Black triangles mark the locations of YJ and ZH radars. The black arrow indicates the direction of environmental VWS. (e) The radius-time Hovmöller diagram of azimuthally averaged radar reflectivity at $z = 2$ km. The black solid line indicates the RMW, and the black dashed line is used to separate stages I and II (see the detail in the text).

the southern side (Figure 2a). This initial configuration demonstrated the azimuthal asymmetry of the inner core at the beginning of the observational period. By 1400 UTC, an eyewall-like structure became clearly discernible. This structure was organized by a convective ring that encircled a cloud-free eye region (Figure 2d). The formation of such a well-defined eyewall-like structure is a clear indication of the transition to a more symmetric inner-core configuration. Concurrent with the convective axisymmetrization of the inner core, Cempaka experienced rapid intensification, as can be observed in Figure 1b. This temporal correlation suggests a potential causal relationship between the formation of the eyewall and the intensification of the storm.

To further examine the convective characteristics associated with the eyewall formation of Cempaka, Figure 2e shows a Hovmöller (radius-time) diagram depicting the azimuthally-averaged radar reflectivity at 2 km altitude. The figure reveals two distinct evolutional phases regarding the eyewall formation: (a) a marked radial outward expansion of reflectivity thresholds exceeding 34 dBZ commencing at 1200 UTC, accompanied by a contraction of the RMW before 1200 UTC and an expansion after 1200 UTC (denoted by the solid black line). (b) Preceding this transition (0900–1200 UTC), enhanced reflectivity values initially emerged inside the RMW before subsequently propagating beyond the RMW. Based on these temporal signatures, we categorize the pre-1200 UTC interval as stage I and the subsequent period as stage II. A detailed examination of convective organization patterns near the RMW revealed the progressive development of narrow spiral rainbands. The following section outlines the characteristics of these spiral structures, with a particular focus on their formation mechanisms, as Cempaka's eyewall developed and the vortex rapidly intensified.

Figures 3a and 3b present azimuth-time diagrams of wavenumber-2 vorticity and reflectivity fields sampled at radii of 18 km (within the RMW) and 35 km (outside the RMW), respectively, at $z = 2$ km. Note that Figure 3a represents stage I, while Figure 3b characterizes stage II. The dynamical relationship between vortex Rossby waves (VRWs) and TC inner rainband activity has been extensively documented (Chen & Yau, 2001; Corbosiero et al., 2006; Li & Wang, 2012a, 2012b; Li et al., 2017; Lin et al., 2018; Montgomery & Kallenbach, 1997; Wang, 2002a, 2002b). It is shown that while cyclonic propagation of wavenumber-2 vorticity and reflectivity signatures persisted through both stages (Figure 3), the wavy structures exhibited marked phase-dependent contrasts. During stage I, a distinct spatial decoupling emerged between the wavenumber-2 reflectivity and vorticity within the RMW, manifesting as a ~60° phase offset (Figure 3a). This misalignment suggests that the rainband activity that contributed to the enhanced convection within the RMW during this phase occurred through

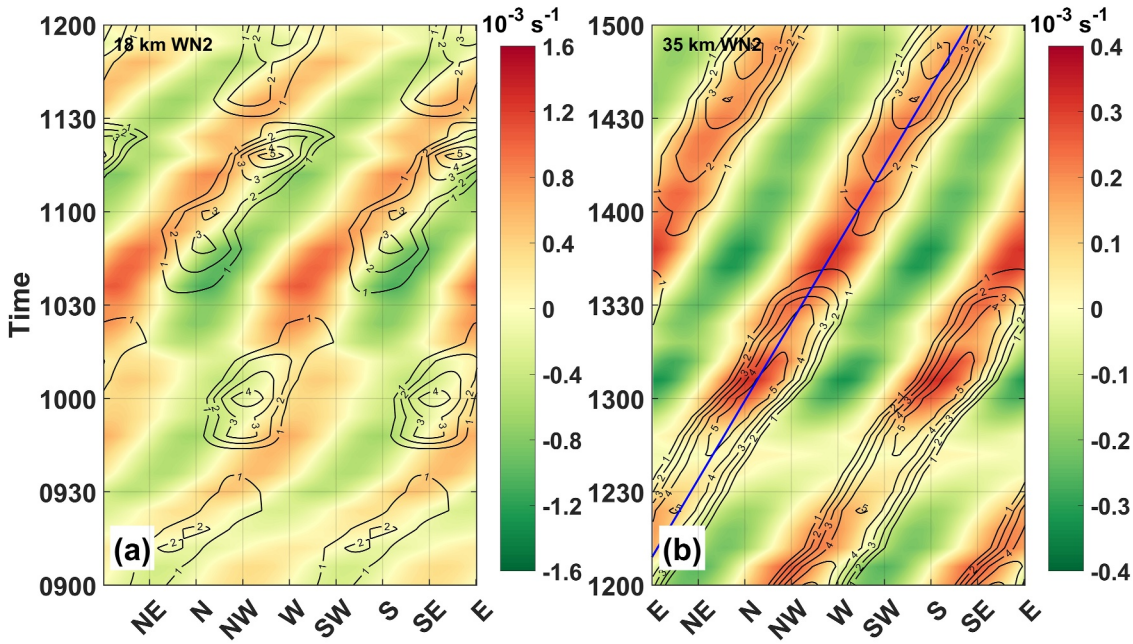

Figure 3. (a) The azimuth-time Hovmöller diagram of wavenumber-2 vorticity (shading; unit: 10^{-3} s^{-1}) and reflectivity (contours; unit: dBZ) at $z = 2$ km at a radius of 18 km from 0900 to 1200 UTC. (b) As for (a) but at a radius of 35 km from 1200 to 1500 UTC. The blue line tracks the cyclonical propagation of wavenumber-2 reflectivity.

mechanisms independent of VRWs dynamics. Conversely, stage II displayed robust phase locking between the wavenumber-2 reflectivity and vorticity exterior to the RMW (Figure 3b), indicative of dynamic coupling consistent with VRWs-driven inner-rainband formation.

Additionally, the azimuthal phase speed of the wavenumber-2 waves, as evaluated from the reflectivity signature shown in Figure 3b, was approximately 18.2 m s^{-1}. In stage II, the average tangential wind speed at a radius of 35 km and an altitude of 2 km was roughly 28.2 m s^{-1}. The azimuthal velocity of the wavenumber-2 structures constituted approximately 65% of the mean tangential wind speed. This result is in accordance with previous studies which indicated that the azimuthal propagation velocity of wavenumber-2 VRWs typically ranged from about 50% to 80% of the local tangential wind velocity (Corbosiero et al., 2006; Dai et al., 2021; Li & Wang, 2012a, 2012b; Lin et al., 2018; Wang, 2002a). In summary, the rainbands within the RMW during stage I were not associated with VRWs. In contrast, the rainbands outside the RMW during stage II could be regarded as convectively coupled VRWs.

Figure 4 presents a comparison of the averaged azimuthal-mean vorticity profiles between the two stages. In stage I, the vorticity skirt exhibited a greater width, whereas in stage II, the profile within the RMW was notably narrower. Specifically, the vorticity within the RMW was substantially higher in stage II compared to stage I. Conversely, outside the RMW, the vorticity was lower in stage II. As previously discussed, this disparity in vorticity distribution gave rise to a more pronounced negative radial gradient, which provided a favorable condition for the development of retrograde VRWs. During stage II, the reduced vorticity outside the RMW allowed the radial inflow to penetrate closer to the center. This circumstance is hypothesized to contribute to more radially inward convergence due to the inflow decelerating around a shorter radius. This observation is consistent with the significant intensification of the typhoon, as evident in Figure 1b, which was observed during stage II.

To elucidate the dynamic difference of rainband-induced convective enhancement within and beyond the RMW during the RI phase (stage I vs. stage II), we compare below fine-scale radar-derived convective organization and kinematic configurations.

One prominent hypothesis suggests that rainbands take shape and propagate as gravity waves. The gravity waves are hypothesized to be generated either by the rotating convective asymmetries within the eyewall region (Kurihara, 1976) or by vorticity perturbations in the core region of the TC (Chow et al., 2002). Here, we aim to

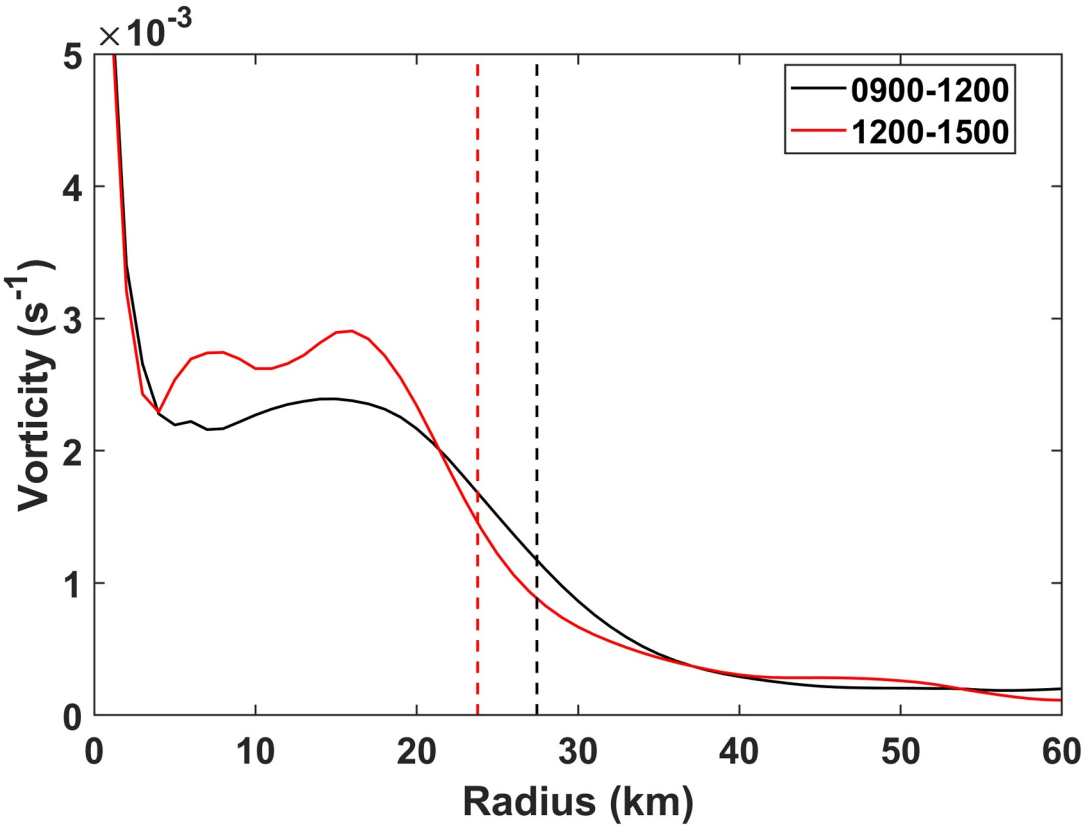

Figure 4. Averaged azimuthal mean vorticity profiles at 2 km altitude in stage I (black) and II (red), respectively. Red and black dashed lines mark the RMW in stages I and II, respectively.

explore whether the propagation of the spiral rainbands inside the RMW during stage I was linked to gravity waves. Figure 5 presents the horizontal distributions of the wavenumber-2 vertical velocity and reflectivity. It is found that the evolution of the wavenumber-2 reflectivity and wavenumber-2 vertical velocity was not collocated. This lack of collocation implies that the rainband during stage I did not exhibit propagation characteristics similar to those of gravity waves. In the context of the theoretical framework of gravity-wave-related rainband propagation, the collocated evolution of the two physical variables is expected. Since the observed wavenumber-2 reflectivity and vertical velocity deviated from this expected pattern, it is reasonable to infer that gravity waves may not be the driving mechanism for the propagation of the spiral rainband inside the RMW during stage I.

To further investigate the underlying mechanisms governing rainband dynamics during stage I, we conduct a focused analysis of spiral rainband B1 (Figures 6e and 6f) within the RMW. The structural organization of B1 appeared intimately linked to the evolution of convective cells C1–C3 (Figures 6a–6d). At 0924 UTC, C1 and C2 were seen in the north and north-northeast, respectively, just outside the RMW (Figure 6a). Retrieved wind fields (Figure 7a) indicated differential strain environments—moderate deformation near C1 versus weaker strain around C2. As C1 moved cyclonically and entered within the RMW, C1 tended to become filamented, possibly influenced by the strain effect (Figure 7b). C2 slightly intensified at 0930 UTC (Figure 6b) and became slightly weaker at 0936 UTC (Figure 6c) when large strain magnitudes on both the upwind and downwind sectors of C2 (Figures 7b and 7c) diluted the cell. Notably, C1 displayed secondary intensification during this phase (Figure 6c), which was probably due to strengthened vortex-scale ascent in downshear quadrants (Bender, 1997; Wang & Holland, 1996). Simultaneously, a nascent convective cell (C3) emerged upstream of C2 (Figure 6c). Temporal evolution over the subsequent 6-min interval revealed progressive intensification and banding of C1 and C2, RMW penetration by C2 (Figure 6d), and vigorous development of C3 within low-strain environments (Figure 7d). The synergistic interaction of filamentation processes and convective coupling ultimately generated inner rainband B1 in the downshear quadrants, radially within the RMW (Figures 6e and 6f). This organizational

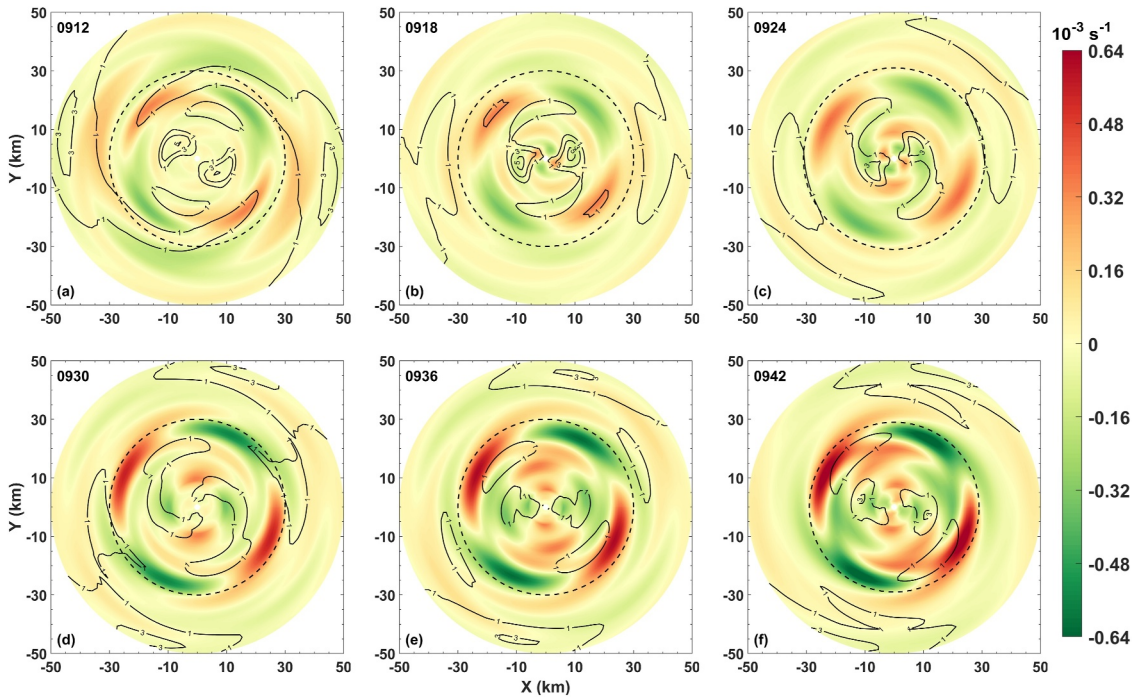

Figure 5. Horizontal distributions of wavenumber-2 vertical velocity (shading; unit: 10^{-3} m s^{-1}) and reflectivity (contours; unit dBZ, solid and dashed lines showing positive and negative parts respectively) at $z = 2$ km every 6 min between 0912 and 0942 UTC. Black dashed lines indicate the RMW.

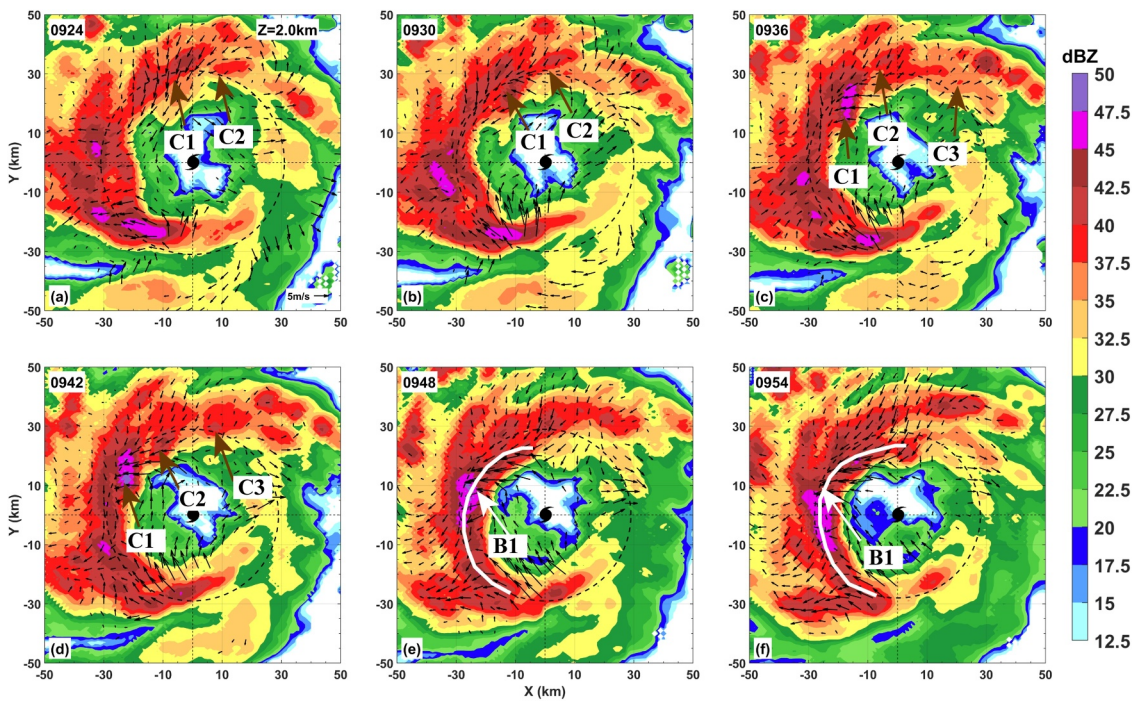

Figure 6. Radar reflectivity (shading; unit: dBZ) at $z = 2$ km at 6-min intervals starting from 0924 UTC, superposed by asymmetric wind fields (vectors). C1, C2, and C3 in panels (a–d) indicate the three convective cells in focus in the text, and B1 in panels (e, f) denotes the inner rainband marked bythe white curve. Black dashed circles indicate the RMW. The time is shown in the top-left cornerof each panel.

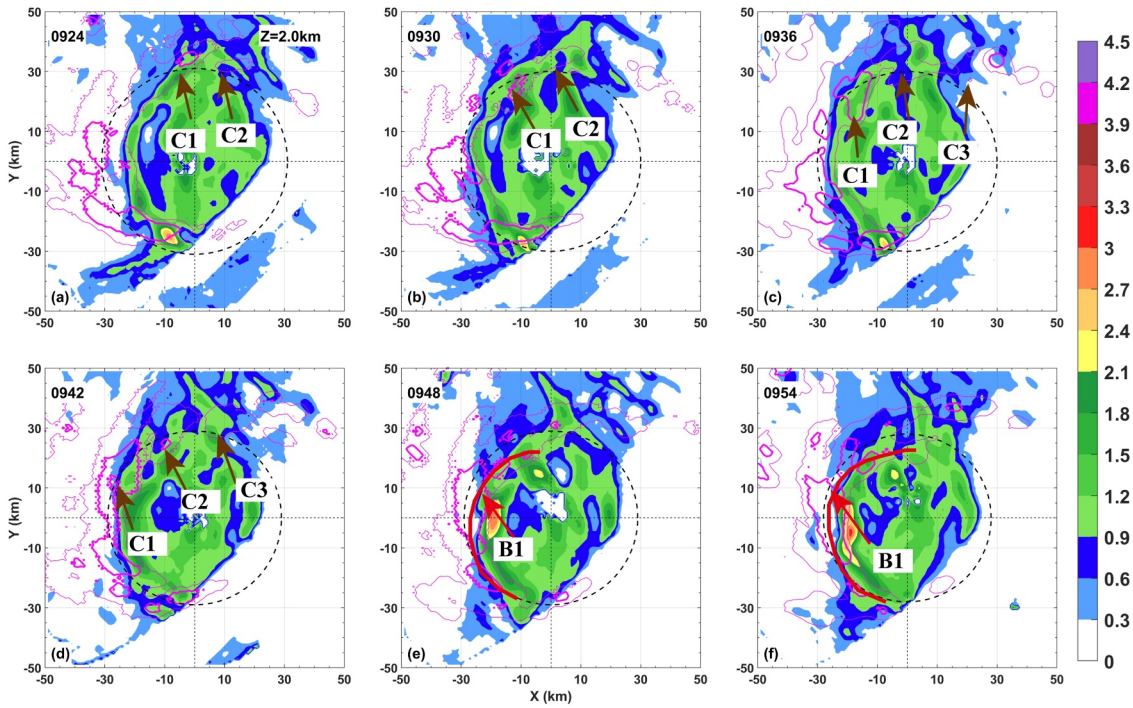

Figure 7. As in Figure 6, but for deformation magnitude (shading) and reflectivity (contoured at 30 and 35 dBZ) at $z = 2$ km. The inner rainband B is marked by the red curve in panels (e, f).

phase coincided with moderate strain conditions (Figures 7e and 7f), preceding the band's transition toward the axisymmetric structure (not shown). The activities of convection described above verified the hypothesis that inner rainbands are formed due to the effect of shear proposed by Moon and Nolan (2015). This structural reorganization amplified convective signatures within the RMW, as evidenced by symmetric radar reflectivity patterns (Figure 2e).

The comprehensive analysis reveals two fundamental characteristics of rainband evolution during stage I of Cempaka's eyewall formation: (a) spatial confinement predominantly within the RMW, and (b) formation mechanisms principally attributable to strain-dominated kinematics. These findings collectively demonstrate remarkable consistency with previous studies (Li et al., 2017; Moon & Nolan, 2015), particularly regarding fine-scale convective reorganization. Specifically, our observational evidence provides empirical validation for the hypothesized process wherein inner-core convective activity undergoes spiral morphogenesis through (a) vorticity-mediated advection within rapid-rotation regimes and (b) subsequent strain-induced deformation, as indicated in the wind field diagnostics performed herein.

To better analyze the wave structures linked to the spiral rainbands beyond the RMW, Figure 8 displays the azimuth–radius distributions of wavenumber-2 radar reflectivity and vertical vorticity at a 2-km altitude during stage II. The above analysis of Typhoon Cempaka's eyewall formation during stage II demonstrates that spiral rainbands located outside the RMW exhibited dynamical coherence with VRWs activity, as manifested through persistent wavenumber-2 banded structures in both radar reflectivity (Figures 3b and 8a–8c) and vorticity (Figures 8d–8f). At 1254 UTC, the radar observations revealed distinct spatial organization: the upwind and mid-sections of an inner rainband (denoted by white lines in Figure 8b) occupied the southwestern quadrant, with its downwind extension propagating eastward, while the counterpart structure displayed mirroring behavior in the northeastern quadrant with westward extension. Figure 8c shows the axisymmetrization of these banded features, culminating in complete eyewall closure. Crucially, the coupling between wavenumber-2 reflectivity patterns and vorticity anomalies at $z = 2$ km (Figures 8d–8f) corroborates the features presented in Figure 3b. This spatio-temporal coherence substantiates that the observed inner rainbands beyond the RMW functioned as convectively coupled VRWs, consistent with the VRWs dynamical frameworks (Chen & Yau, 2001; Li & Wang, 2012a, 2012b; Montgomery & Kallenbach, 1997; Wang, 2002a, 2002b).

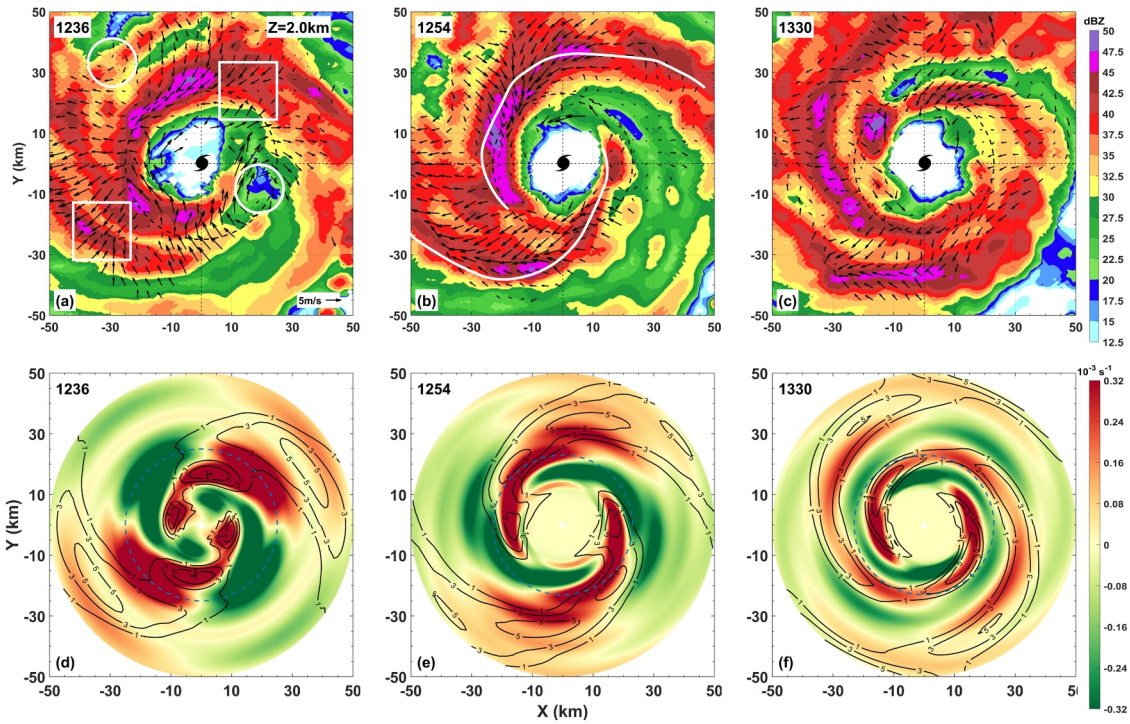

Figure 8. Radar reflectivity (shading; unit: dBZ) at $z = 2$ km at (a) 1236, (b) 1254, and (c) 1306 UTC, overlaid by asymmetric wind fields (vectors). The white curves in panel (b) mark the position of the two inner rainbands discussed in the text. Horizontal distributions of wavenumber-2 vorticity (shading; unit: 10^{-3} s^{-1}) and reflectivity (contours; unit dBZ) at $z = 2$ km are also shown at (d) 1236, (e) 1254, and (f)1306 UTC. Black dashed lines indicate the RMW.

The formation mechanism of VRWs-associated inner rainbands during stage II can be elucidated through dynamical prerequisites and structural evolution. While Montgomery and Kallenbach (1997) documented potential vorticity skirts as fundamental for VRWs genesis, our analysis substitutes vertical vorticity given potential vorticity unavailability, revealing a distinct negative radial vorticity gradient beyond the eyewall (Figure 4). Crucially, wavenumber-2 meso-β-scale cyclone-anticyclone couplets emerged near the eyewall periphery (Figures 8a–8c), with observational evidence at 1236 UTC showing asymmetric anticyclonic vortices in the northwest/southeast quadrants and cyclonic shear-line structures in the northeast/southwest at $z = 2$ km (Figure 8a). This configuration consequently initiated low-level inflow asymmetries beyond a radius of 30 km, likely forced by environmental vertical wind shear. Although the vertical wind shear was weak during this period (Figure 2), Chen et al. (2006) show that asymmetric structures remain detectable even in weak storms, with the asymmetry primarily oriented downshear. As a result, cyclonic shear line-driven outflow convergence was concentrated in the downshear quadrant, establishing a meso-β-scale convergence zone near a radius of 30 km (Figure 8a). The resultant convergence forcing facilitated downshear convective development within the vorticity skirt, ultimately generating wavenumber-2 convectively coupled VRWs (Figures 8d–8f) that physically manifested as the observed inner rainband structures. Furthermore, prior research has also shown the contributions of VRWs to eyewall formation, specifically, secondary eyewall formation. As demonstrated by Guimond et al. (2020) through ground-based and airborne radar measurements, convectively coupled VRWs drive a direct spinup of outer-core tangential winds and exhibit correlation with wavenumber-one secondary eyewall development. The above discussion of the present study specifically examines the axisymmetrization mechanisms of convective-scale VRWs-associated inner bands and their subsequent organization into a coherent eyewall structure during stage II.

The formation of an eyewall manifests through two distinct yet interconnected processes: the development of a ring-like convective structure as previously documented, and the localized intensification of wind fields. During Cempaka's eyewall formation, which coincided with its RI period, a substantial acceleration of wind velocities in proximity to the RMW likely occurred. To elucidate the key dynamical mechanisms governing the wind velocity enhancement processes across both stages, we implemented azimuthally averaged tangential velocity budget

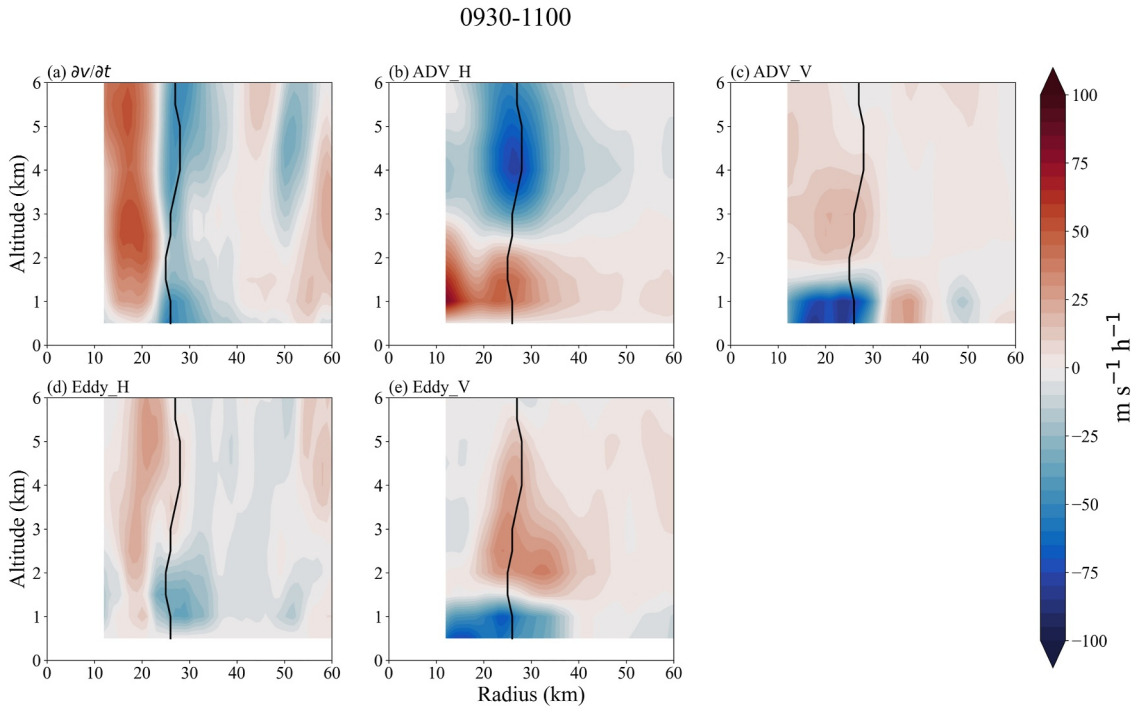

Figure 9. Radius-height cross sections of the azimuthally averaged tangential wind tendency budgets with a 1.5-hr average between 0930 and 1100 in stage I. The budget terms are (a) local time tendency, (b) the mean radial (horizontal) flux of absolute vertical vorticity, (c) the mean vertical advection of mean tangential momentum, (d) the eddy horizontal advection, and (e) the eddy vertical advection of eddy tangential momentum. The temporally averaged RMW is denoted by black solid lines.

analyses as in Tang et al. (2019) and Li et al. (2019). The governing tendency equation within cylindrical coordinates (r, λ, z) can be expressed as follows:

$$\frac{\partial \overline{v}}{\partial t} = -\overline{u}\overline{\zeta_a} - \overline{w}\frac{\partial \overline{v}}{\partial z} - \overline{u'\zeta_a'} - \overline{w'\left(\frac{\partial v'}{\partial z}\right)} - \overline{\frac{\alpha'}{r}\left(\frac{\partial p'}{\partial \lambda}\right)} + \overline{F_{\text{fric}}} + \overline{F_{\text{diff}}}, \quad (1)$$

where u, v, and w are the radial, tangential, and vertical velocities, respectively, $\zeta_a = \frac{\partial v}{\partial r} + \frac{v}{r} + f$ is the vertical component of absolute vorticity, p is pressure, λ indicates the azimuthal angle, α is the specific volume of dry air, t is time, and z is height. The overbar represents the azimuthal mean (the axisymmetric component), and the prime denotes the departure from the azimuthal mean (the asymmetric component). The first four terms on the right-hand side of Equation 1 are the mean radial (horizontal) flux of absolute vertical vorticity, the mean vertical advection of mean tangential momentum, the eddy radial flux of eddy vorticity, and the eddy vertical advection of eddy tangential momentum, respectively. The fifth term is the azimuthal average of the azimuthal perturbation pressure gradient force, which is much smaller than other terms and is ignored in the budget. The last two terms represent turbulent vertical mixing, including surface layer processes and diffusion due to subgrid-scale processes, which are also ignored in the following discussion because they cannot be calculated based on the current data.

Figure 9 shows the azimuthal-mean tangential wind tendency budget during stage I (0930–1100 UTC). Although wind fields below $z = 0.5$ km were poorly resolved due to radar scan coverage limitations, the terms estimated from Equation 1 using the retrieved data still provided helpful quantification for the specific processes driving changes in tangential velocity. A strong positive tangential wind tendency appeared mainly inside the RMW (Figure 9a), directly contributing to its contraction, as shown in Figure 2e. Importantly, below $z = 2.5$ km, the mean radial flux of absolute vorticity showed marked intensification—especially within the RMW (Figure 9b)—and was the dominant factor driving both the acceleration of tangential velocity and the progressive contraction of the RMW. This dominance stemmed primarily from strong boundary-layer inflow (not shown). Furthermore, Figure 4 reveals lower azimuthally averaged vorticity between radii of 5–22 km during stage I than during stage

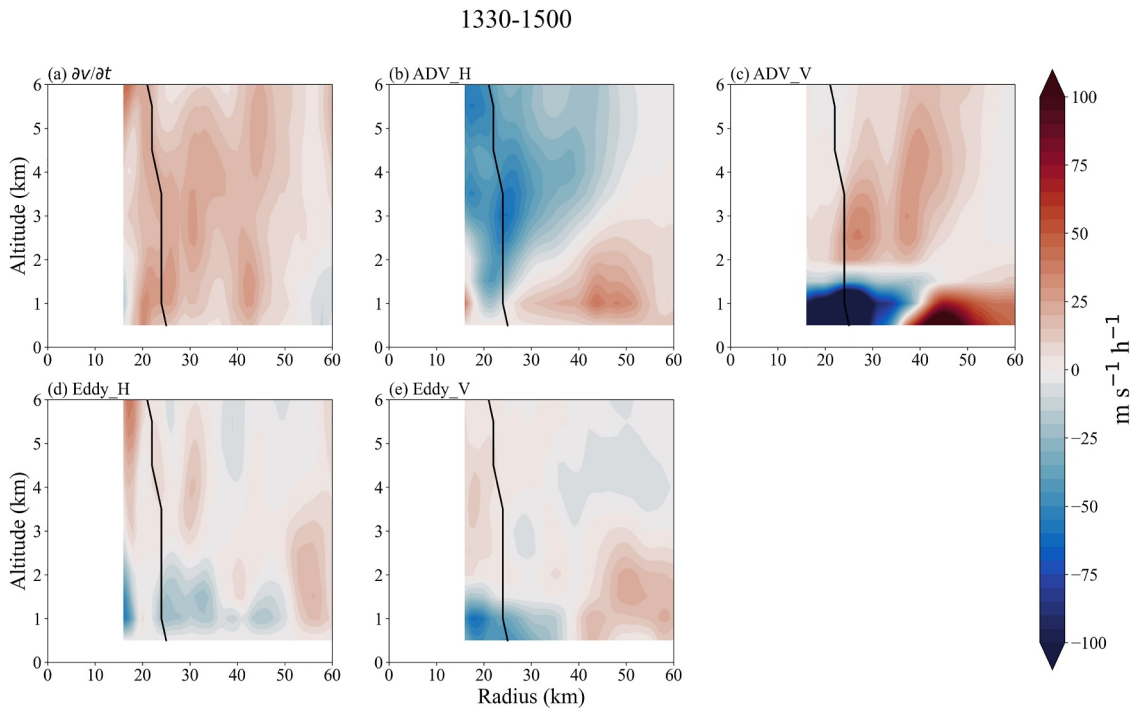

Figure 10. As in Figure 9, but averaged between 1330 and 1500 in stage II.

II, suggesting reduced inertial stability in the early stage. Consequently, the radial inflow likely extended inward to smaller radii during stage I, leading to greater influx of vorticity within the RMW (Rogers et al., 2013).

Additionally, the vertical advection of tangential momentum showed negative tendencies limited to the boundary layer below $z = 1.5$ km, with positive tendencies emerging above $z = 2$ km near and within the RMW (Figure 9c). Notably, horizontal eddy advection produced localized positive tendencies between radii of 12 and 20 km, inside the RMW (Figure 9d), helping to strengthen the tangential winds and drive RMW contraction. The pattern of eddy vertical advection closely mirrored that of mean vertical advection: it reduced tangential velocity at the lower levels ($z < 1.5$ km, $r < 40$ km) while enhancing it aloft (Figure 9e). During stage I, spiral inner rainbands were active within the RMW (Figure 6), which were responsible for positive eddy terms comparable to the radial flux of absolute vorticity inside the RMW; this finding aligns with Hardy et al. (2021) and Alford et al. (2023). Together, these findings indicate that during stage I, the contraction of the RMW was primarily governed by the radial flux of absolute vorticity, while eddy processes linked to inner rainbands and their associated convection within the RMW (Figure 2e) played a secondary—yet still significant—role (Figures 9a–9e).

The tangential wind tendency budgets during stage II (1330–1500 UTC) reveal distinct mechanisms driving tangential wind increases (Figure 10), differing from those in stage I. A broad zone of tangential acceleration developed near and beyond the RMW (Figure 10a), spatially aligned with convective activity in the inner spiral rainbands located outside the RMW. This acceleration around and beyond the RMW was thought to have primarily contributed to the emergence of a local wind maximum during eyewall formation. Compared to stage I (cf. Figure 8), these rainbands exhibited greater axisymmetry, indicating a stronger influence of radial absolute vorticity flux in controlling local wind acceleration below $z = 2$ km and beyond the 40-km radius (Figure 10a). Vertical momentum transport made significant contributions to tangential velocity tendencies above $z = 1.5$ km near and outside the RMW (Figure 10c), counterbalancing the negative effects from radial vorticity flux (Figure 10b). Eddy terms played a relatively minor role compared to mean terms: eddy horizontal advection produced only weak, alternating anomalies (Figure 10d), while eddy vertical advection mainly contributed to low-level acceleration beyond 40 km and below $z = 3$ km (Figure 10e).

4. Conclusions and Discussion

Previous studies have proposed two types of TC eyewall formation from a phenomenological perspective: clearing formation and banding formation (Chen & Wu, 2022), based on satellite imagery. Such results are typically related to the contribution of outer rainband activity to eyewall formation. Nevertheless, further investigation is required to gain insight into the convective behavior of inner rainbands associated with eyewall formation in a TC experiencing RI. This study also aims to investigate the influence of the convective behavior of inner rainbands on the intensity change of TCs during eyewall formation. To address these questions, the convective characteristics regarding the inner rainband activity of Typhoon Cempaka (2021) are observationally examined here using Doppler radars.

The eyewall formation period of interest for Cempaka can be divided into two distinct stages during which the convective activity of the inner rainbands has strikingly different characteristics. In the first stage, spanning from 0900 to 1200 UTC, an azimuthally averaged reflectivity peak was observed to be situated radially inside the RMW of Cempaka. Subsequently, in the second stage, the azimuthally averaged reflectivity peak exhibited a shift, moving outside the RMW.

The development and simultaneous axisymmetrization of the spiral inner rainbands were found to contribute to the eyewall formation of Cempaka and were discussed during both stages of observation. The formation of the inner rainbands in the first stage was closely associated with isolated convection, which ultimately underwent filamentation as a result of strain effects. The mean tangential wind tendency analysis shows that the elevated convection inside the RMW resulted in a net local spin-up within the RMW, particularly due to the eddy terms, thereby contributing to the RMW contraction observed during this stage. In the second stage, the inner rainband activity was predominantly governed by VRWs that were excited outside the RMW. Consequently, an azimuthally averaged reflectivity peak was also observed outside the RMW. The retrieved wind fields indicated that convergence-related convection generated by the interaction between vortex perturbations and low-level asymmetric inflow in the downshear quadrants was the probable cause of the initiation of the VRWs. The subsequent axisymmetrization of the rainbands further contributed to the formation of the eyewall of Cempaka. In this phase, the eddy terms of tangential velocity budgets were observed to be weaker, coupled with an axisymmetric distribution of convection. The positive tangential velocity tendency resulting from the mean terms occurred near and outside the RMW, which was consistent with the development of convection outside the RMW.

In conclusion, the radar observations here suggest that the RI of Typhoon Cempaka was accompanied by the formation of an eyewall. In contrast with the type of banding formation observed from satellite observations, the eyewall formation of Cempaka was linked to the evolution of two distinct types of inner rainbands. In a symmetric view, the principal convection relevant to the deformation-driven inner rainbands and VRWs-associated rainbands was observed to be located inside and outside the RMW, respectively. Although these two types of inner rainbands have been previously identified, the current study emphasizes their potential contribution to the formation of the eyewall of Cempaka and their impact on the marked acceleration of wind velocities near the RMW, particularly from a radar observation view.

While the current study highlights the inner rainband dynamics and its contributions to the eyewall formation of Typhoon Cempaka, previous studies have shown that outer rainbands can also play a role in eyewall/eye formation, as discussed in the introduction section. Could the outer rainbands have contributed to the eyewall formation of Cempaka? Figures 2a–2d show that outer rainbands were located downshear, although the magnitude of the shear tended to decrease with time during the period of interest. Stratiform clouds, indicated by relatively smooth reflectivity distributions, appeared in the downwind sector of the outer rainbands—a characteristic outer rainband pattern of sheared TCs (Li et al., 2017; Liu et al., 2022). We conjecture that this stratiform structure in the outer rainbands was unlikely to directly contribute to the eyewall formation through the banding-type process, given the convective nature of the eyewall. Furthermore, were there interactions between the inner and outer rainbands, and how might such interactions, if present, influence the eyewall formation of Cempaka? The radar-based observations in the current study cannot resolve these questions, and high-resolution numerical simulations will be used in future work to investigate these mechanisms.

We also acknowledge other unexplored aspects stemming from observational constraints inherent in radar observations. Notably, the thermodynamic interplay between inner rainband dynamics and the RI process during Cempaka's eyewall formation remains unquantified. This omission becomes scientifically pertinent given the

documented correlation between organized inner-core convection and TC size expansion. Crucially, as Cempaka exhibited an atypically compact size, this raises the mechanistic question of how convective processes within its inner rainbands modulated both symmetric and asymmetric contributions to size variability. In upcoming studies, such unresolved physical linkages between convective-scale interactions and TC-scale energetics will be investigated through cloud-resolving numerical simulations.

Conflict of Interest

The authors declare no conflicts of interest relevant to this study.

Data Availability Statement

The ERA5 data is publicly available from ECMWF (Hersbach et al., 2023). The radar dataset used to visualize the figures in this paper is available at Fan (2025).

Acknowledgments
This work was jointly supported by the National Natural Science Foundation of China (Grants 42475006, 42192555, 42175005) and Fundamental Research Funds for the Central Universities (No. 020714380171), as well as the Open Grants of the State Key Laboratory of Severe Weather (Grant 2023LASW-A01).

References

Alford, A. A., Biggerstaff, M. I., & Carrie, G. (2023). Using ground-based radar observations to evaluate asymmetric convection and eyewall dynamics during the landfall of Hurricane Harvey (2017). *Journal of the Atmospheric Sciences*, *80*(7), 1867–1889. https://doi.org/10.1175/JAS-D-22-0053.1

Bender, M. A. (1997). The effect of relative flow on the asymmetric structure in the interior of hurricanes. *Journal of the Atmospheric Sciences*, *54*(6), 703–724. https://doi.org/10.1175/1520-0469(1997)054<0703:Teorfo>2.0.Co;2

Black, M. L., & Willoughby, H. E. (1992). The concentric eyewall cycle of Hurricane Gilbert. *Monthly Weather Review*, *120*(6), 947–957. https://doi.org/10.1175/1520-0493(1992)120<0947:TCECOH>2.0.CO;2

Cangialosi, J. P., Blake, E., DeMaria, M., Penny, A., Latto, A., Rappaport, E., & Tallapragada, V. (2020). Recent progress in tropical cyclone intensity forecasting at the national hurricane center. *Weather and Forecasting*, *35*(5), 1913–1922. https://doi.org/10.1175/WAF-D-20-0059.1

Cha, T.-Y., Bell, M. M., & DesRosiers, A. J. (2021). Doppler radar analysis of the eyewall replacement cycle of Hurricane Matthew (2016) in vertical wind shear. *Monthly Weather Review*, *149*(9), 2927–2943. https://doi.org/10.1175/MWR-D-20-0289.1

Chen, G. (2018). Secondary eyewall formation and concentric eyewall replacement in association with increased low-level inner-core diabatic cooling. *Journal of the Atmospheric Sciences*, *75*(8), 2659–2685. https://doi.org/10.1175/jas-d-17-0207.1

Chen, S. S., Knaff, J. A., & Marks, F. D. (2006). Effects of vertical wind shear and storm motion on tropical cyclone rainfall asymmetries deduced from TRMM. *Monthly Weather Review*, *134*(11), 3190–3208. https://doi.org/10.1175/MWR3245.1

Chen, X., Rozoff, C. M., Rogers, R. F., Corbosiero, K. L., Tao, D., Gu, J.-F., et al. (2023). Research advances on internal processes affecting tropical cyclone intensity change from 2018–2022. *Tropical Cyclone Research and Review*, *12*(1), 10–29. https://doi.org/10.1016/j.tcrr.2023.05.001

Chen, X., Wang, Y., Fang, J., & Xue, M. (2018). A numerical study on rapid intensification of Typhoon Vicente (2012) in the South China Sea. Part II: Roles of inner-core processes. *Journal of the Atmospheric Sciences*, *75*(1), 235–255. https://doi.org/10.1175/jas-d-17-0129.1

Chen, Y., & Yau, M. K. (2001). Spiral bands in a simulated hurricane. Part I: Vortex rossby wave verification. *Journal of the Atmospheric Sciences*, *58*(15), 2128–2145. https://doi.org/10.1175/1520-0469(2001)058<2128:sbiash>2.0.co;2

Chen, Y.-L., & Wu, C.-C. (2022). On the two types of tropical cyclone eye formation: Clearing formation and banding formation. *Monthly Weather Review*, *150*(6), 1457–1473. https://doi.org/10.1175/mwr-d-21-0239.1

Chen, Y.-L., & Wu, C.-C. (2025). The impact of outer-core structure on eye formation and intensification of tropical cyclones. *Monthly Weather Review*, *153*(2), 285–308. https://doi.org/10.1175/MWR-D-24-0004.1

Chow, K. C., Chan, K. L., & Lau, A. K. H. (2002). Generation of moving spiral bands in tropical cyclones. *Journal of the Atmospheric Sciences*, *59*(20), 2930–2950. https://doi.org/10.1175/1520-0469(2002)059<2930:GOMSBI>2.0.CO;2

Corbosiero, K. L., Molinari, J., Aiyyer, A. R., & Black, M. L. (2006). The structure and evolution of hurricane Elena (1985). Part II: Convective asymmetries and evidence for vortex rossby waves. *Monthly Weather Review*, *134*(11), 3073–3091. https://doi.org/10.1175/mwr3250.1

Dai, H., Zhao, K., Li, Q., Lee, W.-C., Ming, J., Zhou, A., et al. (2021). Quasi-periodic intensification of convective asymmetries in the outer eyewall of Typhoon Lekima (2019). *Geophysical Research Letters*, *48*(5), e2020GL091633. https://doi.org/10.1029/2020GL091633

Didlake, A. C., Heymsfield, G. M., Reasor, P. D., & Guimond, S. R. (2017). Concentric eyewall asymmetries in Hurricane Gonzalo (2014) observed by airborne radar. *Monthly Weather Review*, *145*(3), 729–749. https://doi.org/10.1175/MWR-D-16-0175.1

Fan, X. (2025). Radar observations of inner rainband contributions to eyewall formation during the rapid intensification of Typhoon Cempaka (2021) (version 1) [Dataset]. *Zenodo*. https://doi.org/10.5281/zenodo.13943460

Fischer, M. S., Reasor, P. D., Dunion, J. P., & Rogers, R. F. (2025). Are rapidly intensifying tropical cyclones associated with unique vortex and convective characteristics? *Monthly Weather Review*, *153*(2), 183–203. https://doi.org/10.1175/MWR-D-24-0118.1

Gall, R., Franklin, J., Marks, F., Rappaport, E. N., & Toepfer, F. (2013). The hurricane forecast improvement project. *Bulletin of the American Meteorological Society*, *94*(3), 329–343. https://doi.org/10.1175/bams-d-12-00071.1

Guimond, S. R., Reasor, P. D., Heymsfield, G. M., & McLinden, M. M. (2020). The dynamics of vortex rossby waves and secondary eyewall development in Hurricane Matthew (2016): New insights from radar measurements. *Journal of the Atmospheric Sciences*, *77*(7), 2349–2374. https://doi.org/10.1175/JAS-D-19-0284.1

Hardy, S., Schwendike, J., Smith, R. K., Short, C. J., Reeder, M. J., & Birch, C. E. (2021). Fluctuations in inner-core structure during the rapid intensification of super Typhoon Nepartak (2016). *Monthly Weather Review*, *149*(1), 221–243. https://doi.org/10.1175/MWR-D-19-0415.1

Helmus, J. J., & Collis, S. M. (2016). The python ARM Radar Toolkit (Py-ART), a library for working with weather radar data in the python programming language. *Journal of Open Research Software*, *4*(1), e25. https://doi.org/10.5334/jors.119

Hendricks, E. A., Peng, M. S., Fu, B., & Li, T. (2010). Quantifying environmental control on tropical cyclone intensity change. *Monthly Weather Review*, *138*(8), 3243–3271. https://doi.org/10.1175/2010mwr3185.1

Hersbach, H., Bell, B., Berrisford, P., Biavati, G., Horányi, A., Muñoz Sabater, J., et al. (2023). ERA5 hourly data on pressure levels from 1940 to present. *Copernicus Climate Change Service (C3S) Climate Data Store (CDS)*. https://doi.org/10.24381/cds.bd0915c6

Houze, R. A. (2010). Clouds in tropical cyclones. *Monthly Weather Review*, *138*(2), 293–344. https://doi.org/10.1175/2009mwr2989.1
Kaplan, J., & DeMaria, M. (2003). Large-scale characteristics of rapidly intensifying tropical cyclones in the North Atlantic Basin. *Weather and Forecasting*, *18*(6), 1093–1108. https://doi.org/10.1175/1520-0434(2003)018<1093:LCORIT>2.0.CO;2
Kaplan, J., Rozoff, C. M., DeMaria, M., Sampson, C. R., Kossin, J. P., Velden, C. S., et al. (2015). Evaluating environmental impacts on tropical cyclone rapid intensification predictability utilizing statistical models. *Weather and Forecasting*, *30*(5), 1374–1396. https://doi.org/10.1175/WAF-D-15-0032.1
Kossin, J. P., & DeMaria, M. (2016). Reducing operational hurricane intensity forecast errors during eyewall replacement cycles. *Weather and Forecasting*, *31*(2), 601–608. https://doi.org/10.1175/WAF-D-15-0123.1
Kossin, J. P., & Eastin, M. D. (2001). Two distinct regimes in the kinematic and thermodynamic structure of the hurricane eye and eyewall. *Journal of the Atmospheric Sciences*, *58*(9), 1079–1090. https://doi.org/10.1175/1520-0469(2001)058<1079:tdritk>2.0.co;2
Kurihara, Y. (1976). On the development of spiral bands in a tropical cyclone. *Journal of the Atmospheric Sciences*, *33*(6), 940–958. https://doi.org/10.1175/1520-0469(1976)033<0940:OTDOSB>2.0.CO;2
Li, Q., & Wang, Y. (2012a). A comparison of inner and outer spiral rainbands in a numerically simulated tropical cyclone. *Monthly Weather Review*, *140*(9), 2782–2805. https://doi.org/10.1175/mwr-d-11-00237.1
Li, Q., & Wang, Y. (2012b). Formation and quasi-periodic behavior of outer spiral rainbands in a numerically simulated tropical cyclone. *Journal of the Atmospheric Sciences*, *69*(3), 997–1020. https://doi.org/10.1175/2011jas3690.1
Li, Q., Wang, Y., & Duan, Y. (2017). A numerical study of outer rainband formation in a sheared tropical cyclone. *Journal of the Atmospheric Sciences*, *74*(1), 203–227. https://doi.org/10.1175/jas-d-16-0123.1
Li, Y., Wang, Y., & Lin, Y. (2019). Revisiting the dynamics of eyewall contraction of tropical cyclones. *Journal of the Atmospheric Sciences*, *76*(10), 3229–3245. https://doi.org/10.1175/JAS-D-19-0076.1
Lin, Y., Li, Y., Li, Q., Chen, M., Xu, F., Wang, Y., & Huang, B. (2018). A long-lasting vortex rossby wave–induced rainband of Typhoon Longwang (2005). *Bulletin of the American Meteorological Society*, *99*(6), 1127–1134. https://doi.org/10.1175/bams-d-17-0122.1
Liu, X., Li, Q., & Dai, Y. (2022). Stronger vertical shear leads to earlier secondary eyewall Formation in idealized numerical simulations. *Geophysical Research Letters*, *49*(10), e2022GL098093. https://doi.org/10.1029/2022GL098093
Miyamoto, Y., & Takemi, T. (2013). A transition mechanism for the axisymmetric spontaneous intensification of tropical cyclones. *Journal of the Atmospheric Sciences*, *70*(1), 112–129. https://doi.org/10.1175/jas-d-11-0285.1
Mohr, C. G., Miller, L. J., Vaughan, R. L., & Frank, H. W. (1986). The merger of mesoscale datasets into a common Cartesian format for efficient and systematic analyses. *Journal of Atmospheric and Oceanic Technology*, *3*(1), 143–161. https://doi.org/10.1175/1520-0426(1986)003<0143:Tmomdi>2.0.Co;2
Montgomery, M. T., & Kallenbach, R. J. (1997). A theory for vortex rossby-waves and its application to spiral bands and intensity changes in hurricanes. *Quarterly Journal of the Royal Meteorological Society*, *123*(538), 435–465. https://doi.org/10.1002/qj.49712353810
Moon, Y., & Nolan, D. S. (2015). Spiral rainbands in a numerical simulation of Hurricane Bill (2009). Part II: Propagation of inner rainbands. *Journal of the Atmospheric Sciences*, *72*(1), 191–215. https://doi.org/10.1175/jas-d-14-0056.1
Nguyen, L. T., & Molinari, J. (2012). Rapid intensification of a sheared, fast-moving hurricane over the Gulf Stream. *Monthly Weather Review*, *140*(10), 3361–3378. https://doi.org/10.1175/mwr-d-11-00293.1
Nolan, D. S., Moon, Y., & Stern, D. P. (2007). Tropical cyclone intensification from asymmetric convection: Energetics and efficiency. (pp. 3377–3405).
Oye, D., & Case, M. (1995). REORDER: A program for gridding radar data. Installation and use manual for the UNIX version. *NCAR/ATD*, *30*.
Oye, R., Mueller, C., & Smith, S. (1995). Software for radar translation, visualization, editing, and interpolation, paper presented at preprints. In *27th conf. on radar meteorology*. American Meteorological Society.
Pendergrass, A. G., & Willoughby, H. E. (2009). Diabatially induced secondary flows in tropical cyclones. Part I: Quasi-steady forcing. *Monthly Weather Review*, *137*(3), 805–821. https://doi.org/10.1175/2008mwr2657.1
Rappaport, E. N., Franklin, J. L., Avila, L. A., Baig, S. R., Beven II, J. L., Blake, E. S., et al. (2009). Advances and challenges at the national hurricane center. *Weather and Forecasting*, *24*(2), 395–419. https://doi.org/10.1175/2008waf2222128.1
Rogers, R., Reasor, P., & Lorsolo, S. (2013). Airborne doppler observations of the inner-core structural differences between intensifying and steady-state tropical cyclones. *Monthly Weather Review*, *141*(9), 2970–2991. https://doi.org/10.1175/mwr-d-12-00357.1
Rozoff, C. M., Velden, C. S., Kaplan, J., Kossin, J. P., & Wimmers, A. J. (2015). Improvements in the probabilistic prediction of tropical cyclone rapid intensification with passive microwave observations. *Weather and Forecasting*, *30*(4), 1016–1038. https://doi.org/10.1175/WAF-D-14-00109.1
Schubert, W. H., & Hack, J. J. (1982). Inertial stability and tropical cyclone development. *Journal of the Atmospheric Sciences*, *39*(8), 1687–1697. https://doi.org/10.1175/1520-0469(1982)039<1687:isatcd>2.0.co;2
Shapiro, L. J., & Willoughby, H. E. (1982). The response of balanced hurricanes to local sources of heat and momentum. *Journal of the Atmospheric Sciences*, *39*(2), 378–394. https://doi.org/10.1175/1520-0469(1982)039<0378:trobht>2.0.co;2
Shimada, U., Aonashi, K., & Miyamoto, Y. (2017). Tropical cyclone intensity change and axisymmetricity deduced from GSMaP. *Monthly Weather Review*, *145*(3), 1003–1017. https://doi.org/10.1175/mwr-d-16-0244.1
Sitkowski, M., Kossin, J. P., & Rozoff, C. M. (2011). Intensity and structure changes during hurricane eyewall replacement cycles. *Monthly Weather Review*, *139*(12), 3829–3847. https://doi.org/10.1175/MWR-D-11-00034.1
Tang, X., Tan, Z.-M., Fang, J., Munsell, E. B., & Zhang, F. (2019). Impact of the diurnal radiation contrast on the contraction of radius of maximum wind during intensification of Hurricane Edouard (2014). *Journal of the Atmospheric Sciences*, *76*(2), 421–432. https://doi.org/10.1175/JAS-D-18-0131.1
Vigh, J. L., Knaff, J. A., & Schubert, W. H. (2012). A climatology of hurricane eye formation. *Monthly Weather Review*, *140*(5), 1405–1426. https://doi.org/10.1175/mwr-d-11-00108.1
Vigh, J. L., & Schubert, W. H. (2009). Rapid development of the tropical cyclone warm core. *Journal of the Atmospheric Sciences*, *66*(11), 3335–3350. https://doi.org/10.1175/2009jas3092.1
Wang, Y. (2002a). Vortex rossby waves in a numerically simulated tropical cyclone. Part I: Overall structure, potential vorticity, and kinetic energy budgets. *Journal of the Atmospheric Sciences*, *59*(7), 1213–1238. https://doi.org/10.1175/1520-0469(2002)059<1213:Vrwian>2.0.Co;2
Wang, Y. (2002b). Vortex rossby waves in a numerically simulated tropical cyclone. Part II: The role in tropical cyclone structure and intensity changes. *Journal of the Atmospheric Sciences*, *59*(7), 1239–1262. https://doi.org/10.1175/1520-0469(2002)059<1239:Vrwian>2.0.Co;2
Wang, Y., & Holland, G. J. (1996). Tropical cyclone motion and evolution in vertical shear. *Journal of the Atmospheric Sciences*, *53*(22), 3313–3332. https://doi.org/10.1175/1520-0469(1996)053<3313:Tcmaei>2.0.Co;2

Willoughby, H. E., Clos, J. A., & Shoreibah, M. G. (1982). Concentric eye walls, secondary wind maxima, and the evolution of the hurricane vortex. *Journal of the Atmospheric Sciences*, *39*(2), 395–411. https://doi.org/10.1175/1520-0469(1982)039<0395:cewswm>2.0.co;2

Willoughby, H. E., & Chelmow, M. B. (1982). Objective determination of hurricane tracks from aircraft observations. *Monthly Weather Review*, *110*(9), 1298–1305. https://doi.org/10.1175/1520-0493(1982)110<1298:Odohtf>2.0.Co;2

Wu, C. C., Wu, S. N., Wei, H. H., & Abarca, S. F. (2016). The role of convective heating in tropical cyclone eyewall ring evolution. *Journal of the Atmospheric Sciences*, *73*(1), 319–330. https://doi.org/10.1175/jas-d-15-0085.1